Nano Research 2024, 17(4): 3130–3138

ISSN 1998-0124 CN 11-5974/O4
https://doi.org/10.1007/s12274-023-6054-7

Template-assisted growth of Co-$BaTiO_3$ vertically aligned nanocomposite thin films with strong magneto-optical coupling effect

Zedong Hu[1], Juanjuan Lu[2], Hongyi Dou[2], Jianan Shen[2], James P. Barnard[2], Juncheng Liu[2], Xinghang Zhang[2], and Haiyan Wang[1,2] (✉)

[1] *School of Electrical and Computer Engineering, Purdue University, West Lafayette, IN 47906, USA*
[2] *School of Materials Engineering, Purdue University, West Lafayette, IN 47906, USA*

Received: 23 May 2023 / **Revised:** 26 July 2023 / **Accepted:** 29 July 2023

ABSTRACT

Oxide-metal based nanocomposite thin films have attracted great interests owing to their unique anisotropic structure and physical properties. A wide range of Au-based oxide-metal nanocomposites have been demonstrated, while other metal systems are scarce due to the challenges in the initial nucleation and growth as well as possible interdiffusions of the metallic nanopillars. In this work, a unique anodic aluminum oxide (AAO) template was used to grow a thin Co seed layer and the following self-assembled metal-oxide (Co-$BaTiO_3$) vertically aligned nanocomposite thin film layer. The AAO template allows the uniform growth of Co-seeds and successfully deposition of highly ordered Co pillars (with diameter < 5 nm and interval between pillars < 10 nm) inside the oxide matrix. Significant magnetic anisotropy and strong magneto-optical coupling properties have been observed. A thin Au-$BaTiO_3$ template was also later introduced for further enhanced nucleation and ordered growth of the Co-nanopillars. Taking the advantage of such a unique nanostructure, a large out-of-plane (OP) coercive field (H_c) of ~ 5000 Oe has been achieved, making the nanocomposite an ideal candidate for high density perpendicular magnetic tunneling junction (p-MTJ). A strong polar magneto-optical Kerr effect (MOKE) has also been observed which inspires a novel optical-based reading method of the MTJ states.

KEYWORDS

vertically aligned nanocomposite (VAN), Co, $BaTiO_3$, thin film, magneto-optical coupling, magnetic anisotropy

1 Introduction

Hybrid oxide-metal metamaterials have attracted tremendous interest in the past decades for the tunable physical properties and multifunctionalities toward emerging technologies [1–24]. For example, self-assembled epitaxial Au-$BaTiO_3$ (BTO) hybrid nanostructures have shown to have tailorable Au pillar morphology, density and tunable optical and ferroelectric properties [1, 3, 6, 9, 12, 25]. Following these initial demonstrations, a range of Au-based oxide-metal nanocomposites have been demonstrated, including Au-ZnO [5], Au-ZnO-BTO [4, 8], and Au-$LiNbO_3$ [2]. The first ferromagnetic metal-dielectric oxide nanocomposite structure was demonstrated in Ni-$BaZrYO_3$ system [24] with very strong magnetic anisotropy and broad magnetic property tuning demonstrated. Following that, Fe-$BaTiO_3$ and Co-$BaZrO_3$ systems have also been demonstrated [15, 18, 19, 22]. Beside single metal nanopillars, various alloyed systems have been explored, including Ag_xAu_{1-x}-ZnO alloy for significantly reduced optical loss [7], Au-Fe-BTO core–shell structures for obvious magneto-plasmonic coupling properties [13]. Besides these, other metal pillars (e.g., Cu-oxide, Pt-oxide, and Al-oxide systems) have also been tested with great potentials [26–28].

In terms of the fabrication of the oxide-metal hybrid metamaterials, some of the most popular approaches are lithography patterning [29], focused ion beam (FIB) and e-beam patterning [30], and electroplating of the metal nanopillars using an anodized alumina template [31]. These approaches can be used to process nanoscale metal structures as fine as tens of nanometers and in highly ordered fashion, despite the challenges in scaling up to wafer scale processing. As an alternative approach, a simple one-step self-assembly method using pulsed lase deposition (PLD) has been demonstrated to deposit a wide range of metal-oxide vertically aligned nanocomposite (VAN) thin films [12, 32, 33] with potential for future wafer-scale integration. Despite the versatile two-phase oxide-oxide [34–41], oxide-metal [3, 6, 42] , and nitride-metal VAN [43–45] systems demonstrated so far, the fundamental nucleation and growth mechanisms of the two phase systems are still under investigation [32, 46–50]. For example, the two-phase distributions are found to be uniform overall, but still quite random without specific ordering. Several approaches have been explored for guided nucleation and growth of VAN systems, including the surface treated $SrTiO_3$ substrates for guided growth of $La_{0.7}Sr_{0.3}MnO_3$-CeO_2 system and $La_{0.7}Sr_{0.3}MnO_3$-Au system [10, 16], and FIB based seeding growth of $CoFe_2O_4$ pillars in $BiFeO_3$ matrix [51]. These methods require either specific substrates or a nanoscale patterning step. Clearly, a more versatile seeding

---

Address correspondence to hwang00@purdue.edu

method is thus needed for a more controlled nucleation and growth of the two-phase VAN systems.

In this work, we introduce a new seeding method using an anodized alumina template to seed the metal nanopillar growth in oxide-metal VANs. For this demonstration, we selected the Co-BTO VAN system on $SrTiO_3$ (STO) (001). Co is known as a typical ferromagnetic material and a plasmonic metal, and $BaTiO_3$ is a well-studied perovskite oxide with nonlinear optical response and strong ferroelectric properties. Combining the two in VAN form, one can expect combined ferromagnetic and ferroelectric properties, anisotropic optical and magnetic properties, as well as potential magneto-optical coupling because of the well-integrated multi-functionalities in one material system. The specific templating method is illustrated in Fig. 1. Specifically, three different deposition processes are demonstrated and compared: (1) a regular one-step self-assembled approach of Co-BTO VAN (a direct deposition), (2) a Co-BTO VAN on an Au-BTO template, and (3) a Co seed layer growth using anodic aluminum oxide (AAO) template followed by the Co-BTO deposition. Interestingly, these three different deposition methods significantly change the growth mechanism and morphologies of Co nanostructures from randomly distributed nanoinclusions to highly ordered nanopillars embedded in matrix. The magnetic and optical properties, and magneto-optical coupling properties were measured and compared for the three cases to show the effects of seeding on the overall nucleation and growth of the nanostructures, and thus tuning the geometry and physical properties of the oxide-metal metamaterials.

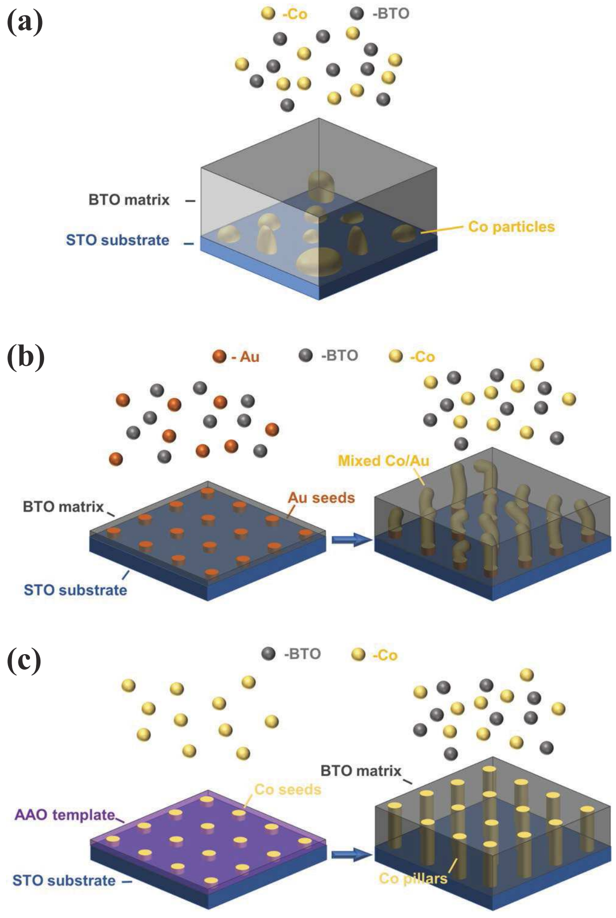

Figure 1 Schematics of (a) direct deposition of BTO/Co VAN on STO (001), (b) deposition of BTO/Co VAN on STO (001) with BTO/Au template and (c) deposition of BTO/Co on STO(001) while seeding Co at first with AAO template.

2 Results and discussion

As shown in the scanning transmission electron microscopy images taken under the high-angle annular dark-field mode (STEM-HAADF) and TEM images along with electron dispersive X-ray spectroscopy (EDS) in Figs. 2(a2)–2(a4), in the Co-BTO system using the direct deposition method, the Co nanostructures only nucleated as small nanoparticles (~ 8 nm in diameter) at the interface of BTO on STO substrate without obvious pillar formation in the BTO matrix. This morphology is quite different compared to other metal-oxide systems previously reported (e.g., Co-CeO_2-BTO, Au-BTO, Au-LSMO, etc.) [1, 6, 10, 21], which all present obvious metal pillars in the oxide matrix through the self-assembly process. This suggests the challenging nucleation process of Co nanopillars in BTO matrix. The initial nucleation and growth of oxide-metal VAN involve many factors, including 1) different growth rates of metal and oxide phases, 2) different surface energy of metal and oxide phases, 3) difference in adatom diffusion rates, and 4) lattice mismatch between the metal, the matrix, and the substrate. When adatoms arrive at the substrate, metal and oxide behave quite differently because of their different surface energies. Typically, oxides have lower or comparable surface energy compared to the oxide substrates and thus result in layered growth. While metals have higher surface energy than that of the oxide substrate which results in an island growth of metal onto the substrate. Hence, metal-oxide nanocomposites can grow as VAN thin films. This mechanism has been proven in many cases (Au-$BaTiO_3$, Au-CeO_2, Fe-$BaTiO_3$, etc.) [4, 18, 52]. However, it is not the case for the Co-BTO growth. As shown in Fig. 2(a4), the direct deposition of Co-BTO resulted in the uniform growth of Co-doped BTO film, despite multiple deposition attempts. This is perhaps related to the very high surface energy of Co. An effective approach to overcome this challenge could be to deposit a template to facilitate the Co nanopillar formation. The first template adopted in this work is the Au-BTO template. The advantage of templating methods over the direct deposition is that the template can work as a buffer layer itself (e.g., Au-BTO template) or help to deposit metal seeds on the substrate. The buffer layer, or the metal seeds could provide preferred nucleation sites for the newly incoming Co adatoms. Apparently, the growth of Au-BTO as a buffer helped the nucleation of the Co pillars, as evidenced from Figs. 2(b2)–2(b5). Obvious Co nanoparticles and nanocolumns are forming in the BTO matrix. It is interesting to note that Co and Au grew as well mixed nanostructures different from the immiscible metals prediction and phase separation seen in other BTO-multi-metal VAN systems [13, 53].

The above data suggests that the Au-BTO template did not seed the Co-BTO growth well and thus we have grown the Co-BTO VAN film with the assistance of AAO template. The pore diameter of the AAO template ranges from 20 to 250 nm. To seed the metal onto the substrate and then grow metal-oxide VAN thin film, one should consider the template with pore diameter comparable or slightly larger than the metal pillar diameter. In our case, an AAO template with pore diameter of 20 nm was selected since the diameter of Co pillar is usually less than 10 nm. Larger pore diameter may lead to excess metal seeding on substrates. After the seeding Co on STO substrate using AAO template, we then deposited Co-BTO films on top of the templated substrate. Very different from the direct Co-BTO and the Au-BTO buffered cases, the AAO templated Co-BTO shows very obvious Co nanopillar growth in the BTO matrix, evidenced in Fig. 3. This set of STEM and EDS images suggest that the average diameter of the Co pillars is of ~ 3 nm and all pillars are highly ordered and grow vertically. The cross-sectional EDS results of Ba/Co and Co shown

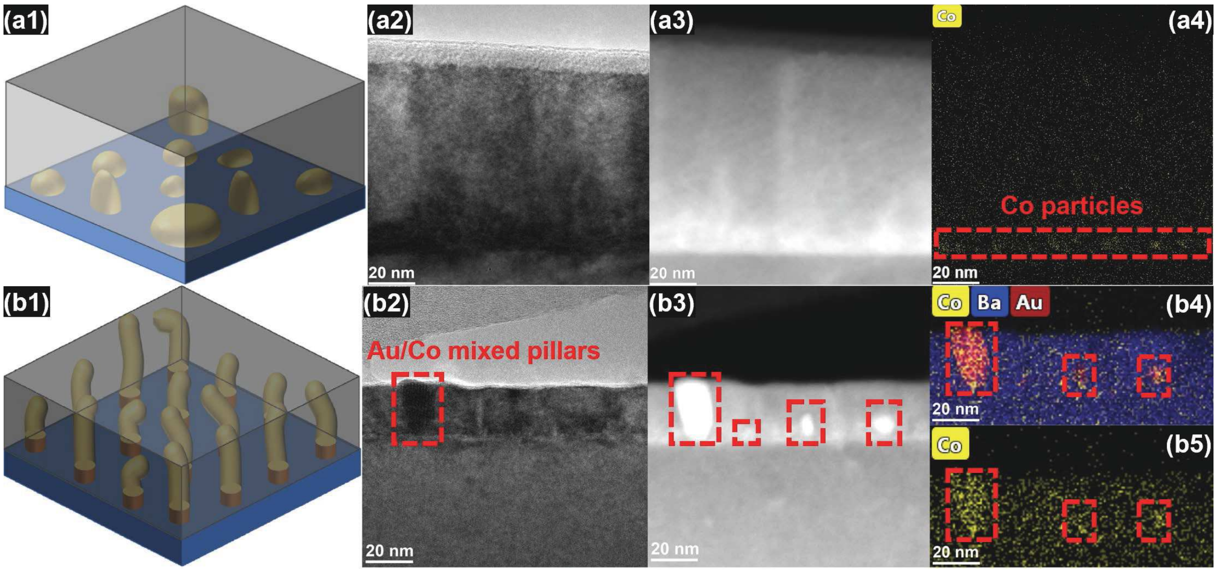

Figure 2 (a1)–(a4) Microstructure study of directly deposited Co-BTO VAN thin film while (a1) corresponding schematic illustration of cross-sectional TEM image, (a2) TEM image, (a3) STEM image and (a4) EDS results of Co. (b1)–(b5) Microstructure study of Co-BTO VAN thin film deposited with BTO/Au template while (b1) corresponding schematic illustration of cross-sectional TEM image, (b2) TEM image, (b3) STEM image, (b4) EDS mapping of Ba/Au/Co, and (b5) EDS mapping of Co.

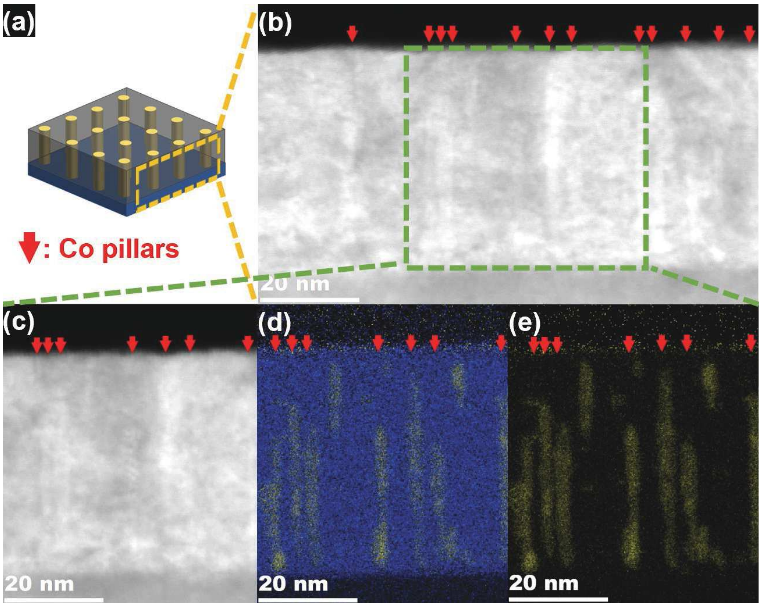

Figure 3 Microstructure study of Co-BTO VAN thin film deposited with assistance of AAO template. (a) Corresponding schematic illustration of cross-sectional TEM image, (b) STEM image of Co-BTO VAN thin film deposited with AAO template, (c) HAADF image of selected area from (b), (d) EDS mapping of Co/Ba, and (e) EDS mapping of Co for corresponding area.

in Figs. 3(d) and 3(e), suggest the formation of a two-phase nanocomposite system with clear and sharp interfaces, despite minor Co diffusion in the BTO matrix. In addition, at the interface of the thin film and the substrate, a few Co seeds were observed which were formed at the first step of AAO templated Co deposition. The dependence of Co nanostructure on pulse number has been investigated as well. The EDS mappings of Co for Co-BTO VAN thin films deposited with different laser pulse numbers are shown in Fig. S1 in the Electronic Supplementary Material (ESM). The pulse number significantly changes the nanostructure of Co in the BTO matrix.

The crystallinity of Co-BTO VAN thin film was also characterized by X-ray diffraction (XRD). The full XRD θ–2θ patterns of Co-BTO thin films deposited by three different methods on STO substrates are shown in the left panel of Fig. 4. The XRD results for Co-BTO VAN thin films deposited with different pulse numbers are shown in Fig. S2 in the ESM. The STO substrate (a = 3.905 Å) was selected regarding its close lattice mismatching with $BaTiO_3$ (a = 3.992 Å) and hence benefited the epitaxial growth of Co-BTO film. The XRD results show the highly textured growth of $BaTiO_3$ along the (100) orientation. For Co-BTO deposited using Au-BTO template, Au (111) and Au (222) peaks are both identified. The broad BTO (002) peak indicates the overlapping with Au (002) peak due to the similar lattice parameters which is corresponding with the previous report [54]. The right panel of Fig. 4 shows the local detailed XRD θ–2θ plot with the scan range from 40° to 50°. It is worth noting that the BTO (002) peak shifts due to the lattice mismatch and strain in the nanostructures. BTO (002) peak for the film using the direct deposition method stays at the original peak position (~ 44.926°) since it does not present obvious VAN structures. The one deposited with the Au-BTO template has its BTO (002) peak shift to right. As shown in Fig. 2(b4), Co and Au grow as mixed pillars embedded in the BTO matrix. The lattice parameters of Au (a_{Au} =

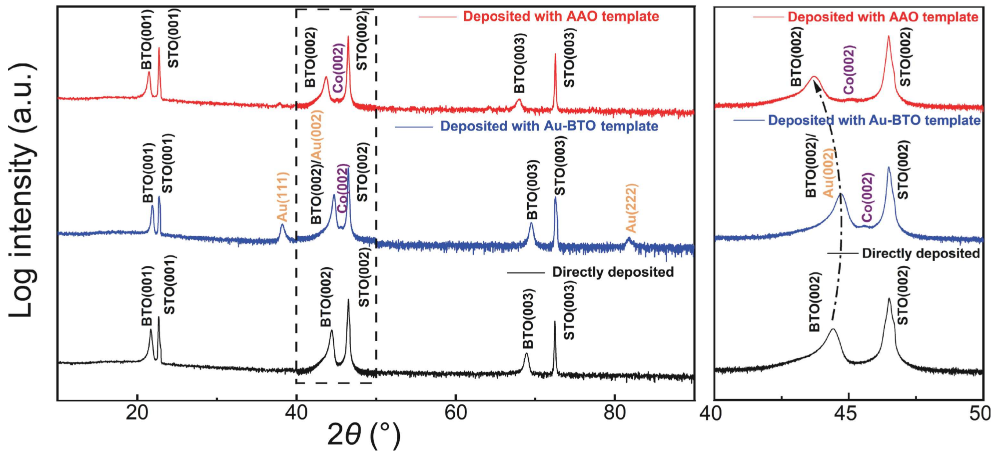

Figure 4 XRD results. The left panel displays full XRD θ–2θ patterns of samples with different deposition methods on STO (001) substrate. The right panel shows local detailed XRD θ–2θ plot with scan range from 40° to 50°.

4.0786 Å) and Co (c_{Co} = 4.07 Å) are both greater than that of BTO (a_{BTO} = 4.031 Å) which shall result in tensile strain in BTO and shall result in a left shift of the peak. The slightly compressive strain in BTO for the Au-BTO template one might be due to the well mixed Au-Co lattice with a smaller average lattice parameter. A cubic Co lattice is reported to be 3.51 Å. The film deposited with AAO template shows a more obvious peak shift to left since the hcp Co lattice parameter (c_{Co} = 4.07 Å) is larger than that of BTO. The strain between the Co and BTO suggests the better vertically coupled Co nanopillars in BTO matrix deposited with AAO template. It's also clearly shown in the right panel of Fig. 4 that the Co peaks are mostly buried in between the BTO (200) and STO (200) peaks for Co-BTO VAN thin films deposited with templates.

The key characteristic of the Co-BTO VAN thin film is the combined magnetic and optical functionalities including plasmonic, anisotropic optical and magnetic properties. The optical transmittance spectra of Co-BTO thin films deposited with the three different deposition methods were collected using a depolarized incident light as shown in Fig. 5(b). The obvious transmittance valleys represent light absorption demonstrating the broad plasmonic resonance attributed to the Co nanostructure. It is obvious that for all Co-BTO films deposited by different methods, the localized surface plasmon resonance (LSPR) peaks occur at ~ 465 and ~ 514 nm, which agrees well with the previous reports. Note that the peaks may appear a blue shift slightly because of the strain generated at the interfaces of BTO and Co. The absorption intensity is strongest for the AAO templated sample and drops for the Au-BTO buffered and the direct deposited ones. The two absorption valleys could be resulted from the different Co nanostructures inside the Co-BTO VAN thin film, i.e., nanopillars, vs. nanoparticles. The dielectric constants were fitted and presented in Fig. 5(a). The obtained data of Co-BTO VAN thin films was modeled as in-plane ($\varepsilon'_{//}$) and out-of-plane ($\varepsilon'_{\perp}$) component using the general oscillator models (Kramers–Kronig Model). Because of the well-fined two-phase metal-oxide VAN structure and hence introduced anisotropic structure, a hyperbolic region between 1800 and 2000 nm was observed for Co-BTO VAN thin film only deposited with AAO template. For the one deposited with Au-BTO template, as the EDS results shown in Fig. 2(b4), the Au grows more like bulks instead of pillars. This makes the film has less optics anisotropy. In the hyperbolic region, the out-of-plane ($\varepsilon'_{\perp}$) component of the dielectric constant becomes negative while in-plan ($\varepsilon'_{//}$) component keeps positive. The anisotropic optical property makes the Co-BTO VAN thin film an ideal hyperbolic metamaterial for future photonic applications.

The magnetic properties of the Co-BTO VAN thin films were also measured to investigate their potential applications ranging from data storage to permanent magnets. The M–H measurements of all Co-BTO thin film were conducted with applied external magnetic field in-plane (IP) and out-of-plane (OP) to the films at both room temperature (300 K) and low temperature (10 K). The results are shown in Fig. 6. Figures 6(a1)–6(c1) show the M–H loops at 10 K, while Figs. 6(a2)–6(c2) show the M–H loops at 300 K for all Co-BTO VAN thin films deposited with different methods. Insets at top left corner are the schematic illustration of magnetic properties measurement. The insets at bottom right corner are the enlargement of selected area to identify the coercivity field.

In the figure, all red solid lines with squares indicate the OP data while black solid lines with triangles indicate the IP data,

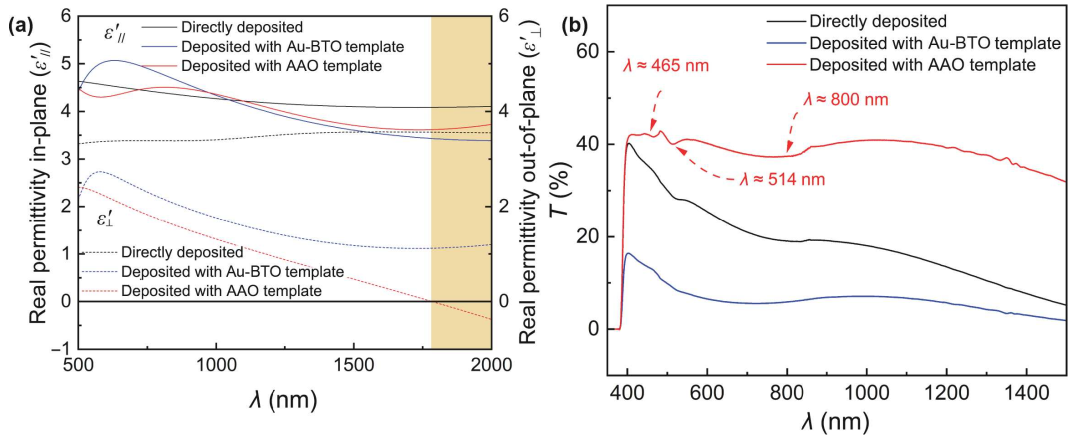

Figure 5 (a) Real part of the in-plane ($\varepsilon'_{//}$) and out-of-plane ($\varepsilon'_{\perp}$) permittivity, and (b) Transmittance of Co-BTO VAN thin films deposited with different methods.

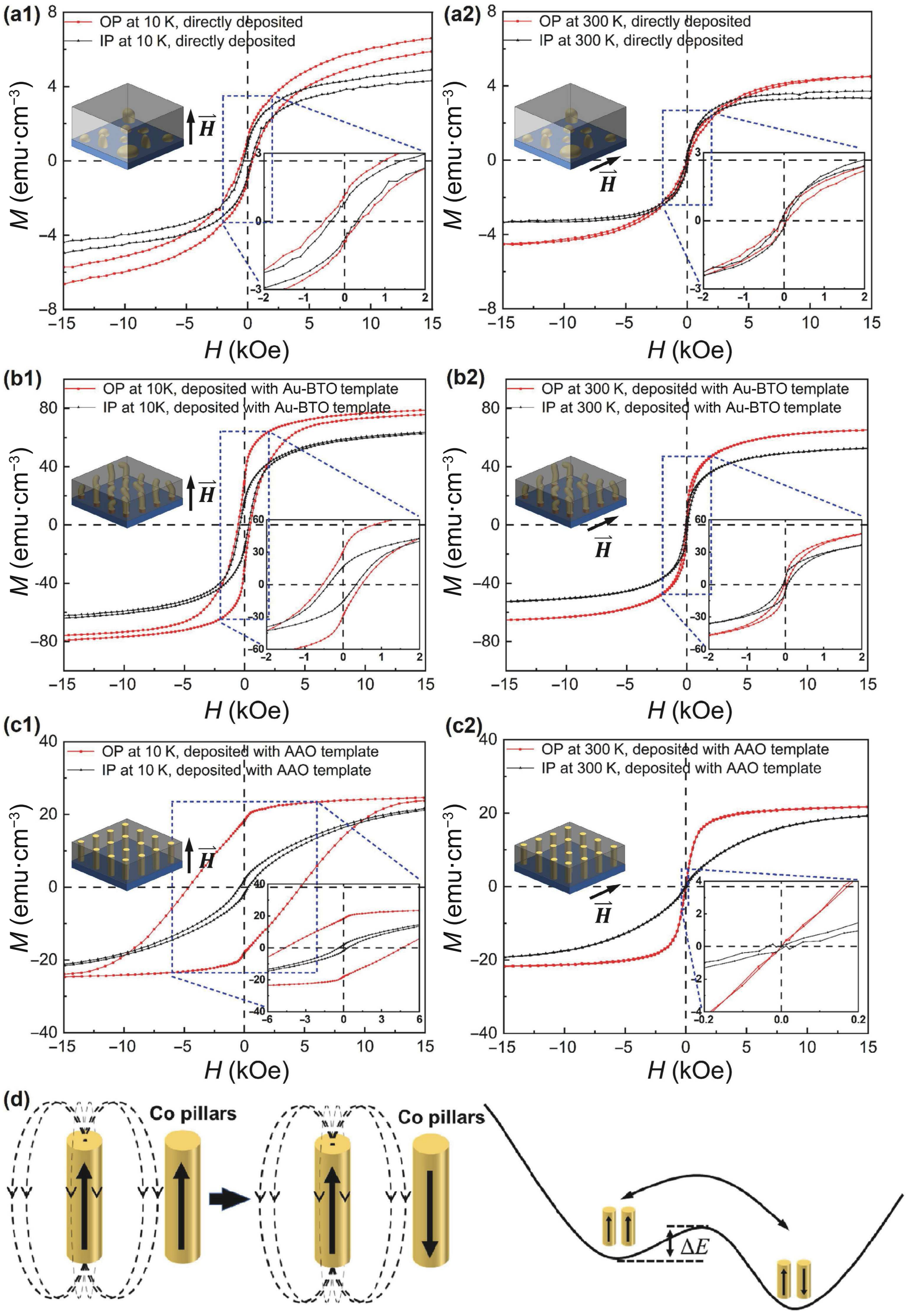

Figure 6 (a1)–(c1) The *M*–*H* loops at 10 K for Co-BTO VAN thin films deposited with three different methods respectively. (a2)–(c2) The *M*–*H* loops at 300 K for Co-BTO VAN thin films deposited with three different methods respectively. Insets at top left corner show the schematic of the magnetic properties measurement. Insets at bottom right corner represent the enlargement of the selected area to identify the coercivity field. (d) Schematic of switching of magnetic orientation.

respectively. Note that the unit of magnetization (y-axis) here is emu·cm^{-3}, it is not surprising that the M_s of all samples are not as high as expected since the volume divided is the entire volume of the film. It is intuitively expected that films deposited either directly or with BTO/Au template should not have very much magnetic anisotropy since previous results have shown that films deposited by those two methods do not have well-defined Co nanostructures. Figures 6(a1) and 6(a2) represent the data of the directly deposited sample for IP and OP at 10 K and room temperature (300 K), respectively. The magnetic susceptibilities (χ) are generally the same for IP and OP even at low temperature. The inset of Fig. 6(a1) shows the *M*–*H* loop at low temperature near the low field from which it is obvious that even the coercivity for IP and OP does not change. As we recall from Figs. 2(a2)–2(a4), for the directly deposited sample, most of the Co grew as nanoparticles at the interface of the thin film and substrate, but not the obvious pillars as seen in Figs. 2(b2)–2(b5) and Fig. 3. Obviously, the magnetic properties of the Co-BTO VAN system vary based on the morphology of the Co. The shape effect is believed to be one of the key factors controlling the magnetic properties of films. Regarding the particle-like growth of the Co, it might not introduce significant magnetic anisotropy due to the isotropic Co nanostructures. It is also worth noting that the coercivity of all samples at low temperatures is larger than that at room temperature while the M_s behaves quite the opposite. The reason is that thermodynamic effects always favor the switching of the magnetic orientation. Furthermore, M–H loops for Co-BTO VAN thin films deposited with different pulse numbers have been collected and plotted in Fig. S3 in the ESM. The results show the magnetic anisotropy of the film can be easily tuned by changing the Co nanostructures.

Figures 6(b1) and 6(b2) indicate the M–H loops of the sample deposited with Au-BTO template for IP and OP at 10 K and 300 K. The results are similar to the sample deposited directly which shows no significant magnetic anisotropy. The magnetic susceptibility and coercivity are nearly unchanged for IP and OP since the nanostructures are rod-like. Figures 6(c1) and 6(c2) represent the M–H loops for sample deposited with AAO template for IP and OP at 10 and 300 K. It clearly shows that this sample has a significant magnetic anisotropy compared to the other two. At room temperature, the coercivity for both IP and OP is quite small while the magnetic susceptibility changes significantly. The magnetic easy axis of the Co nanopillars is always along the pillar direction. As shown in Fig. 6(d), at room temperature, the Co pillars will feel demagnetization from others. Besides, thermal effect becomes stronger at room temperature. Both factors together make it easier to switch the magnetic orientation at room temperature and reduce the coercivity field (H_c). While at low temperature, thermodynamic effect becomes weak making it harder to switch the magnetic orientation of the single domain. This significantly increases the coercivity (~ 5 kOe) for OP just as was observed from Fig. 6(c1). For nanopillars, it is intuitive that coercivity of metal strongly depends on its geometric features such as diameter and length. For example, Whitney et al. reported that coercivity field of nickel nanowires increases with the decreasing diameter, due to the generation of multi-domains in the nanowire with a larger diameter [55]. Huang et al. also reported that the coercivity of Co-BaZrO$_3$ VAN thin film decreases with decreasing the Co pillar diameter [15]. The reason is that Co nanopillars with small diameters ($d < d_c$, d_c is defined as Eq. (1)) can be regarded as single-domain magnetic structures and coherent rotation mode is implemented. Furthermore, the height of the nanopillars also dominates the magnetic anisotropy (e.g., H_c) of the film by changing its shape anisotropy (or aspect ratio of the nanopillars). The M–H loops for films deposited with AAO template with different height of the nanopillars were shown in the ESM. These indicate that coercivity increases as we increased the height of the nanopillars.

$$d_c = 2\sqrt{\frac{kA}{\mu_0 M_s^2}} \tag{1}$$

Interestingly, the Co-BTO film deposited with the AAO template has both plasmonic effects and magnetic anisotropy. Consequently, we investigated the magneto-optic effect of the sample. Figure 7 shows the magneto-optic Kerr effect (MOKE) results of the sample at room temperature for (a) the polar (out of plane) θ_k–H loop and (b) the longitudinal (in plane) θ_k–H loop. The insets indicate the schematic of the measurement setup. There also exists a large anisotropy in the MOKE results for OP and IP. The OP θ_k is easily saturated (at ~ 1500 Oe) and the value is much larger than the IP value, which is far from saturated applying a similar external magnetic field. This is due to the change in polarization from the system symmetry upon reflection at a magnetic surface. Such a change resulted from the dielectric tensor of the film with an external magnetic field which is shown below

$$\overset{\leftrightarrow}{\varepsilon} = \begin{bmatrix} \varepsilon_0 & i\varepsilon_z & -i\varepsilon_y \\ -i\varepsilon_z & \varepsilon_0 & i\varepsilon_x \\ i\varepsilon_y & -i\varepsilon_x & \varepsilon_0 \end{bmatrix} \tag{2}$$

where $\varepsilon_i = \varepsilon_0 Q m_i$ ($i = x$, y, and z), Q is the Voigt magneto optical constant and m_i is the ratio between the magnitude of magnetization in a given direction and the magnitude of saturated magnetization of the sample $m_i = M_i/M_s$. Based on our previous discussions, at room temperature, the magnetic susceptibility for OP is much larger than that for IP making the OP magnetization easier to get saturated. Therefore ε_z can be easily changed at low field leading to a larger θ_k for OP. This allows the magnetic orientation of the sample to be detected using polarized light which can be used as the reading technology of next-generation MTJ in the future.

With the assistance of the AAO template, we successfully deposited a highly ordered two-phase Co-BTO VAN thin film. Ultra-thin Co nanopillars grow vertically inside the BTO matrix, forming well fined Co/BTO interfaces. Despite of some limitations of the AAO template including its fragile nature, dimensional variations, and requirement for additional cleaning process, using AAO template to seed metal can promote the initial metal nucleation and improve the film nanostructure. As a feasibility demonstration for seeded growth of VAN using AAO template, this opens the possibility for highly ordered pillar growth rather than the completely random growth of the metal nanopillars. Compared with other Co-based VAN system or Co based nanostructure, for example, Co-BaZrO$_3$ [15], the as-deposited Co-BTO VAN thin film in this work shows both magnetic and optical anisotropy, as well as magneto-optical coupling effects which have not been achieved previously. The films display a large coercivity field of ~ 5 kOe at low temperature as well as large susceptibility at room temperature and reach its saturation magnetization at an applied field of ~ 2 kOe. The large coercivity field makes the film a potential candidate for perpendicular magnetic recording medium

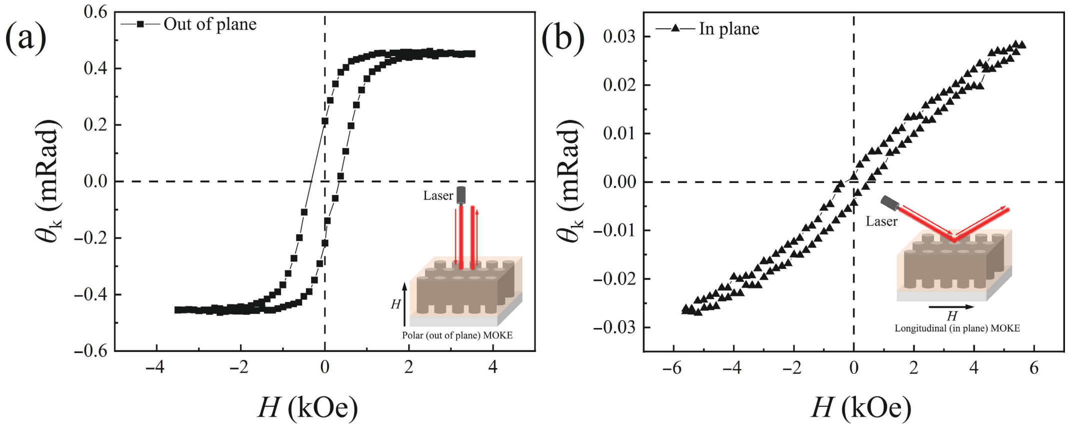

Figure 7 MOKE results of Co-BTO VAN thin film deposited with AAO template. (a) shows Polar (out of plane) MOKE results while (b) shows Longitudinal (in plane) MOKE results respectively. Insets are the schematics of the measurement respectively.

applications. Besides, such a ferromagnetic (Co)-ferroelectric (BTO) based VAN system raises great interest in further investigation on its magnetoelectric coupling effect. Taking advantage of the plasmonic nature of Co and its pillar-like structure, Co-BTO VAN thin film also displays optical anisotropy and suggests a hyperbolic region beyond 1800 nm. This makes the Co-BTO VAN thin film a promising candidate for future optical applications. Furthermore, the MOKE anisotropy makes it possible to use polarized light as the novel MTJ reading approach for next generation MRAM.

3 Conclusion

In this work, the implementation of AAO template has been proven to be an effective method of initiating and controlling the Co-nanopillar growth in Co-BTO nanocomposite thin film. This process was conducted using the PLD deposition of Co-seed layer via the AAO template with well controlled growth parameters. With the AAO templated Co deposition, the following Co-BTO VAN thin films exhibit high epitaxial quality for both Co and BTO phases. The microstructure analysis yields well-defined Co nanopillars embedded in the BTO matrix making the coercivity of the sample tunable. Additionally, large magnetic susceptibility at room temperature and notable magneto-optic Kerr effects make the vertically aligned Co-BTO thin film a very promising candidate for p-MTJ and introduces the potential to use polarized light as a MTJ reading technology.

4 Experimental section

Thin film fabrication: The Co-BTO composite target was made of a pure BTO target and Co strips. The self-assembled thin films were deposited under vacuum using pulsed laser deposition (with a KrF excimer laser, $\lambda = 248$ nm). For directly deposited Co-BTO thin film, the sample was fabricated on single crystalline STO (001) substrate using the PLD system. For thin film deposited with Au-BTO template, Au-BTO buffer layer was firstly deposited on single crystalline STO (001) substrate. Then the Co-BTO layer was deposited on top of the Au-BTO buffer layer with a Co-BTO target. For sample deposited with AAO template, the Co was first deposited with pure Co sheet and AAO template to form Co seeds on single crystalline STO (001) substrate. The AAO template method includes the following steps: cleaning of the AAO template, attaching the AAO template on substrates, and depositing Co nanoseed layer. Then Co-BTO was deposited on top of the templated substrate using Co-BTO target. The laser beam was focused on the target surface with an incident angle of 45° and laser energy about 3.6 $\text{J}\cdot\text{m}^{-2}$. The distance between the target and substrate was around 4.5 cm. The base chamber was pumped to lower than 1.0×10^{-6} mTorr to provide a desired vacuum atmosphere. The deposition temperature was optimized at 700 °C and deposition frequency was 2 Hz. After deposition, the samples were cooled down at the rate of 15 $°\text{C}\cdot\text{min}^{-1}$ to room temperature under vacuum.

Microstructure characterization: The crystallinity and microstructure of the films were characterized by XRD (Panalytical X'Pert X-ray diffractometer with Cu $K\alpha$ radiation), TEM, STEM and EDS for chemical mapping (FEI Talos F200X). TEM samples were prepared by a standard procedure, including grinding, polishing, dimpling and ion milling (PIPS 691, Gatan Inc).

Optical measurement: Depolarized transmittance (T%) spectra was measured using a ultraviolet visible-near infrared (UV–vis–NIR) absorption spectrophotometer (Perkin Elmer Lambda 1050).

Magnetic and Kerr measurement: Magnetic hysteresis loops were collected using a magnetic property measurement system (MPMS) from Quantum Design. Vibrating sample magnetometer (VSM) mode with a superconducting quantum interface device (SQUID) sensor was applied for high accuracy. A home-built MOKE system with a He-Ne laser at 632.8 nm was used for room temperature Kerr measurements. The incident light was polarized using a linear polarizer, and the Kerr rotation was measured using a second polarizer assisted by a photoelastic modulator. For polar configuration, the reflected light was separated from the normal incident light by a 50% beam splitter, with a magnetic field perpendicular to the film surface. For longitudinal mode, the laser impinged at approximately 30° incidence, and the magnetic field was parallel to the film surface.

Acknowledgement

The work is funded by the U.S. Department of Energy, Office of Science, Basic Energy Sciences with award No. DE-SC0020077. The TEM/HRSTEM work was supported by the U.S. National Science Foundation DMR-2016453. This paper describes objective technical results and analysis. Any subjective views or opinions that might be expressed in the paper do not necessarily represent the views of the U.S. Department of Energy or the United States Government.

Electronic Supplementary Material: Supplementary material (EDS maps of Co, XRD results, and the M–H loops for Co-BTO VAN thin films using the template assisted deposition method with different thicknesses) is available in the online version of this article at https://doi.org/10.1007/s12274-023-6054-7.

References

[1] Li, L. G.; Sun, L. Y.; Gomez-Diaz, J. S.; Hogan, N. L.; Lu, P.; Khatkhatay, F.; Zhang, W. R.; Jian, J.; Huang, J. J.; Su, Q. et al. Self-assembled epitaxial Au-oxide vertically aligned nanocomposites for nanoscale metamaterials. *Nano Lett.* **2016**, *16*, 3936–3943.

[2] Huang, J. J.; Jin, T. N.; Misra, S.; Wang, H.; Qi, Z. M.; Dai, Y. M.; Sun, X.; Li, L. G.; Okkema, J.; Chen, H. T. et al. Tailorable optical response of Au-LiNbO_3 hybrid metamaterial thin films for optical waveguide applications. *Adv. Opt. Mater.* **2018**, *6*, 1800510.

[3] Kalaswad, M.; Zhang, D.; Gao, X.; Contreras, L. L.; Wang, H.; Wang, X.; Wang, H. Integration of hybrid plasmonic Au-BaTiO_3 metamaterial on silicon substrates. *ACS Appl. Mater. Interfaces* **2019**, *11*, 45199–45206.

[4] Misra, S.; Li, L. G.; Zhang, D.; Jian, J.; Qi, Z. M.; Fan, M.; Chen, H. T.; Zhang, X. H.; Wang, H. Y. Self-assembled ordered three-phase Au-BaTiO_3-ZnO vertically aligned nanocomposites achieved by a templating method. *Adv. Mater.* **2019**, *31*, 1806529.

[5] Paldi, R. L.; Sun, X.; Wang, X. J.; Zhang, X. H.; Wang, H. Y. Strain-driven in-plane ordering in vertically aligned ZnO-Au nanocomposites with highly correlated metamaterial properties. *ACS Omega* **2020**, *5*, 2234–2241.

[6] Zhang, D.; Qi, Z. M.; Jian, J.; Huang, J. J.; Phuah, X. L.; Zhang, X. H.; Wang, H. Y. Thermally stable Au-BaTiO_3 nanoscale hybrid metamaterial for high-temperature plasmonic applications. *ACS Appl. Nano Mater.* **2020**, *3*, 1431–1437.

[7] Paldi, R. L.; Wang, X. J.; Sun, X.; He, Z. H.; Qi, Z. M.; Zhang, X. H.; Wang, H. Y. Vertically aligned $\text{Ag}_x\text{Au}_{1-x}$ alloyed nanopillars embedded in ZnO as nanoengineered low-loss hybrid plasmonic metamaterials. *Nano Lett.* **2020**, *20*, 3778–3785.

[8] Misra, S.; Zhang, D.; Qi, Z. M.; Li, D. F.; Lu, J. J.; Chen, H. T.; Wang, H. Y. Morphology control of self-assembled three-phase Au-BaTiO_3-ZnO hybrid metamaterial for tunable optical properties. *Cryst. Growth Des.* **2020**, *20*, 6101–6108.

[9] Liu, J. C.; Wang, X. J.; Gao, X. Y.; Wang, H.; Jian, J.; Huang, J. J.; Sun, X.; Qi, Z. M.; Misra, S.; He, Z. H. et al. Multifunctional self-

assembled $BaTiO_3$-Au nanocomposite thin films on flexible mica substrates with tunable optical properties. *Appl. Mater. Today* **2020**, *21*, 100856.

[10] Lu, J.; Paldi, R. L.; Pachaury, Y.; Zhang, D.; Wang, H.; Kalaswad, M.; Sun, X.; Liu, J.; Phuah, X. L.; Zhang, X. et al. Ordered hybrid metamaterial of $La_{0.7}Sr_{0.3}MnO_3$-Au vertically aligned nanocomposites achieved on templated $SrTiO_3$ substrate. *Mater. Today Nano* **2021**, *15*, 100121.

[11] Huang, J. J.; Wang, H.; Qi, Z. M.; Lu, P.; Zhang, D.; Zhang, B.; He, Z. H.; Wang, H. Y. Multifunctional metal-oxide nanocomposite thin film with plasmonic Au nanopillars embedded in magnetic $La_{0.67}Sr_{0.33}MnO_3$ matrix. *Nano Lett.* **2021**, *21*, 1032–1039.

[12] Zhang, D.; Wang, H. Y. Self-assembled metal-dielectric hybrid metamaterials in vertically aligned nanocomposite form with tailorable optical properties and coupled multifunctionalities. *Adv. Photonics Res.* **2021**, *2*, 2000174.

[13] Rutherford, B. X.; Dou, H. Y.; Zhang, B.; He, Z. H.; Barnard, J. P.; Paldi, R. L.; Wang, H. Y. Single-step fabrication of Au-Fe-$BaTiO_3$ nanocomposite thin films embedded with non-equilibrium Au-Fe alloyed nanostructures. *Nanomaterials* **2022**, *12*, 3460.

[14] Zhang, D.; Gao, X. Y.; Lu, J. J.; Lu, P.; Deitz, J.; Shen, J. N.; Dou, H. Y.; He, Z. H.; Shang, Z. X.; Wade, C. A. et al. Novel self-assembled two-dimensional layered oxide structure incorporated with Au nanoinclusions towards multifunctionalities. *Nano Res.* **2023**, *16*, 1465–1472.

[15] Huang, J. J.; Li, L. G.; Lu, P.; Qi, Z. M.; Sun, X.; Zhang, X. H.; Wang, H. Y. Self-assembled Co-$BaZrO_3$ nanocomposite thin films with ultra-fine vertically aligned Co nanopillars. *Nanoscale* **2017**, *9*, 7970–7976.

[16] Fan, M.; Zhang, B.; Wang, H.; Jian, J.; Sun, X.; Huang, J. J.; Li, L. G.; Zhang, X. H.; Wang, H. Y. Self-organized epitaxial vertically aligned nanocomposites with long-range ordering enabled by substrate nanotemplating. *Adv. Mater.* **2017**, *29*, 1606861.

[17] Huang, J. J.; Qi, Z. M.; Li, L. G.; Wang, H.; Xue, S. C.; Zhang, B.; Zhang, X. H.; Wang, H. Y. Self-assembled vertically aligned Ni nanopillars in CeO_2 with anisotropic magnetic and transport properties for energy applications. *Nanoscale* **2018**, *10*, 17182–17188.

[18] Zhang, B.; Huang, J.; Rutherford, B. X.; Lu, P.; Misra, S.; Kalaswad, M.; He, Z.; Gao, X.; Sun, X.; Li, L. et al. Tunable, room-temperature multiferroic Fe-$BaTiO_3$ vertically aligned nanocomposites with perpendicular magnetic anisotropy. *Mater. Today Nano* **2020**, *11*, 100083.

[19] Kalaswad, M.; Zhang, B.; Wang, X. J.; Wang, H.; Gao, X. Y.; Wang, H. Y. Integration of highly anisotropic multiferroic $BaTiO_3$-Fe nanocomposite thin films on Si towards device applications. *Nanoscale Adv.* **2020**, *2*, 4172–4178.

[20] Wang, X. J.; Qi, Z. M.; Liu, J. C.; Wang, H. H.; Xu, X. S.; Zhang, X. H.; Wang, H. Y. Strong interfacial coupling of tunable Ni-NiO nanocomposite thin films formed by self-decomposition. *ACS Appl. Mater. Interfaces* **2021**, *13*, 39730–39737.

[21] Rutherford, B. X.; Zhang, B.; Kalaswad, M.; He, Z. H.; Zhang, D.; Wang, X. J.; Liu, J. C.; Wang, H. Y. Tunable three-phase Co-CeO_2-$BaTiO_3$ hybrid metamaterials with nano-mushroom-like structure for tailorable multifunctionalities. *ACS Appl. Nano Mater.* **2022**, *5*, 6297–6304.

[22] Liu, J. C.; Wang, X. J.; Gao, X. Y.; Wang, H.; Zhang, B.; Zhang, D.; Kalaswad, M.; Huang, J. J.; Wang, H. Y. Integration of self-assembled $BaZrO_3$-Co vertically aligned nanocomposites on mica substrates toward flexible spintronics. *Cryst. Growth Des.* **2022**, *22*, 718–725.

[23] Paldi, R. L.; Kalaswad, M.; Lu, J. J.; Barnard, J. P.; Richter, N. A.; Si, M. W.; Bhatt, N. A.; Ye, P. D.; Sarma, R.; Siddiqui, A. et al. ZnO-ferromagnetic metal vertically aligned nanocomposite thin films for magnetic, optical and acoustic metamaterials. *Nanoscale Adv.* **2023**, *5*, 247–254.

[24] Su, Q.; Zhang, W. R.; Lu, P.; Fang, S. M.; Khatkhatay, F.; Jian, J.; Li, L. G.; Chen, F. L.; Zhang, X. H.; MacManus-Driscoll, J. L. et al. Self-assembled magnetic metallic nanopillars in ceramic matrix with anisotropic magnetic and electrical transport properties. *ACS Appl. Mater. Interfaces* **2016**, *8*, 20283–20291.

[25] Zhang, D.; Lu, P.; Misra, S.; Wissel, A.; He, Z. H.; Qi, Z. M.; Gao, X. Y.; Sun, X.; Liu, J. C.; Lu, J. J. et al. Design of 3D oxide-metal hybrid metamaterial for tailorable light-matter interactions in visible and near-infrared region. *Adv. Opt. Mater.* **2021**, *9*, 2001154.

[26] Huang, J.; Wang, X.; Phuah, X. L.; Lu, P.; Qi, Z.; Wang, H. Plasmonic Cu nanostructures in ZnO as hyperbolic metamaterial thin films. *Mater. Today Nano* **2019**, *8*, 100052.

[27] Masuda, T.; Fukumitsu, H.; Fugane, K.; Togasaki, H.; Matsumura, D.; Tamura, K.; Nishihata, Y.; Yoshikawa, H.; Kobayashi, K.; Mori, T. et al. Role of cerium oxide in the enhancement of activity for the oxygen reduction reaction at Pt-CeO_x nanocomposite electrocatalyst - an *in situ* electrochemical X-ray absorption fine structure study. *J. Phys. Chem. C* **2012**, *116*, 10098–10102.

[28] Pyo, S.; Eom, W.; Kim, Y. J.; Lee, S. H.; Han, T. H.; Ryu, W. H. Super-expansion of assembled reduced graphene oxide interlayers by segregation of Al nanoparticle pillars for high-capacity Na-Ion battery anodes. *ACS Appl. Mater. Interfaces* **2020**, *12*, 23781–23788.

[29] Melosh, N. A.; Boukai, A.; Diana, F.; Gerardot, B.; Badolato, A.; Petroff, P. M.; Heath, J. R. Ultrahigh-density nanowire lattices and circuits. *Science* **2003**, *300*, 112–115.

[30] Gansel, J. K.; Thiel, M.; Rill, M. S.; Decker, M.; Bade, K.; Saile, V.; Von Freymann, G.; Linden, S.; Wegener, M. Gold helix photonic metamaterial as broadband circular polarizer. *Science* **2009**, *325*, 1513–1515.

[31] Yao, J.; Liu, Z. W.; Liu, Y. M.; Wang, Y.; Sun, C.; Bartal, G.; Stacy, A. M.; Zhang, X. Optical negative refraction in bulk metamaterials of nanowires. *Science* **2008**, *321*, 930.

[32] Misra, S.; Wang, H. Y. Review on the growth, properties and applications of self-assembled oxide-metal vertically aligned nanocomposite thin films-current and future perspectives. *Mater. Horiz.* **2021**, *8*, 869–884.

[33] Wang, X. J.; Wang, H. Y. Recent advances in vertically aligned nanocomposites with tunable optical anisotropy: Fundamentals and beyond. *Chemosensors* **2021**, *9*, 145.

[34] Chen, A. P.; Bi, Z. X.; Tsai, C. F.; Lee, J.; Su, Q.; Zhang, X. H.; Jia, Q. X.; MacManus-Driscoll, J. L.; Wang, H. Y. Tunable low-field magnetoresistance in $(La_{0.7}Sr_{0.3}MnO_3)_{0.5}$: $(ZnO)_{0.5}$ self-assembled vertically aligned nanocomposite thin films. *Adv. Funct. Mater.* **2011**, *21*, 2423–2429.

[35] Khatkhatay, F.; Chen, A. P.; Lee, J. H.; Zhang, W. R.; Abdel-Raziq, H.; Wang, H. Y. Ferroelectric properties of vertically aligned nanostructured $BaTiO_3$-CeO_2 thin films and their integration on silicon. *ACS Appl. Mater. Interfaces* **2013**, *5*, 12541–12547.

[36] Fan, M.; Zhang, W. R.; Jian, J.; Huang, J. J.; Wang, H. Y. Strong perpendicular exchange bias in epitaxial $La_{0.7}Sr_{0.3}MnO_3$: $LaFeO_3$ nanocomposite thin films. *APL Mater.* **2016**, *4*, 076105.

[37] Gao, X. Y.; Li, L. G.; Jian, J.; Huang, J. J.; Sun, X.; Zhang, D.; Wang, H. Y. Tunable low-field magnetoresistance properties in $(La_{0.7}Ca_{0.3}MnO_3)_{1-x}$: $(CeO_2)_x$ vertically aligned nanocomposite thin films. *Appl. Phys. Lett.* **2019**, *115*, 053103.

[38] Gao, X. Y.; Zhang, D.; Wang, X. J.; Jian, J.; He, Z. H.; Dou, H. Y.; Wang, H. Y. Vertically aligned nanocomposite $(BaTiO_3)_{0.8}$: $(La_{0.7}Sr_{0.3}MnO_3)_{0.2}$ thin films with anisotropic multifunctionalities. *Nanoscale Adv.* **2020**, *2*, 3276–3283.

[39] Huang, J. J.; Wang, H.; Wang, X. J.; Gao, X. Y.; Liu, J. C.; Wang, H. Y. Exchange bias in a $La_{0.67}Sr_{0.33}MnO_3$/NiO heterointerface integrated on a flexible mica substrate. *ACS Appl. Mater. Interfaces* **2020**, *12*, 39920–39925.

[40] Dou, H. Y.; Gao, X. Y.; Zhang, D.; Dhole, S.; Qi, Z. M.; Yang, B.; Hasan, M. N.; Seo, J. H.; Jia, Q. X.; Hellenbrand, M. et al. Electroforming-free HfO_2: CeO_2 vertically aligned nanocomposite memristors with anisotropic dielectric response. *ACS Appl. Electron. Mater.* **2021**, *3*, 5278–5286.

[41] Li, L. G.; Misra, S.; Gao, X. Y.; Liu, J. C.; Wang, H.; Huang, J. J.; Zhang, B.; Lu, P.; Wang, H. Y. Novel vertically aligned nanocomposite of Bi_2WO_6-Co_3O_4 with room-temperature multiferroic and anisotropic optical response. *Nano Res.* **2021**, *14*, 4789–4794.

[42] Zhang, Y. Z.; Zhang, D.; Liu, J. C.; Lu, P.; Deitz, J.; Shen, J. N.; He, Z. H.; Zhang, X. H.; Wang, H. Y. Self-assembled HfO_2-Au nanocomposites with ultra-fine vertically aligned Au nanopillars.

Nanoscale **2022**, *14*, 11979–11987.

[43] Song, J.; Zhang, D.; Lu, P.; Wang, H.; Xu, X.; Meyerson, M. L.; Rosenberg, S. G.; Deitz, J.; Liu, J.; Wang, X. et al. Anisotropic optical and magnetic response in self-assembled TiN-CoFe$_2$ nanocomposites. *Mater. Today Nano* **2023**, *22*, 100316.

[44] Kalaswad, M.; Zhang, D.; Rutherford, B. X.; Lu, J. J.; Barnard, J. P.; He, Z. H.; Liu, J. C.; Wang, H. H.; Xu, X. S.; Wang, H. Y. TiN-Fe vertically aligned nanocomposites integrated on silicon as a multifunctional platform toward device applications. *Crystals* **2022**, *12*, 849.

[45] Wang, X. J.; Jian, J.; Wang, H. H.; Liu, J. C.; Pachaury, Y.; Lu, P.; Rutherford, B. X.; Gao, X. Y.; Xu, X. S.; El-Azab, A. et al. Nitride-oxide-metal heterostructure with self-assembled core–shell nanopillar arrays: Effect of ordering on magneto-optical properties. *Small* **2021**, *17*, 2007222.

[46] Huang, J. J.; MacManus-Driscoll, J. L.; Wang, H. Y. New epitaxy paradigm in epitaxial self-assembled oxide vertically aligned nanocomposite thin films. *J. Mater. Res.* **2017**, *32*, 4054–4066.

[47] Starkey, K.; Ahmad, A.; Lu, J. J.; Wang, H. Y.; El-Azab, A. A generalized 3D elastic model for nanoscale, self-assembled oxide-metal thin films with pillar-in-matrix configurations. *Acta Mater.* **2022**, *228*, 117779.

[48] Chen, A. P.; Jia, Q. X. A pathway to desired functionalities in vertically aligned nanocomposites and related architectures. *MRS Bull.* **2021**, *46*, 115–122.

[49] Zhang, D.; Kalaswad, M.; Wang, H. Self-assembled vertically aligned nanocomposite systems integrated on silicon substrate: Progress and future perspectives. *J. Vac. Sci. Technol. A* **2022**, *40*, 010802.

[50] Wang, X. J.; Wang, H. Y. Self-assembled nitride-metal nanocomposites: Recent progress and future prospects. *Nanoscale* **2020**, *12*, 20564–20579.

[51] Comes, R.; Liu, H. X.; Khokhlov, M.; Kasica, R.; Lu, J. W.; Wolf, S. A. Directed self-assembly of epitaxial CoFe$_2$O$_4$-BiFeO$_3$ multiferroic nanocomposites. *Nano Lett.* **2012**, *12*, 2367–2373.

[52] Lu, J. J.; Zhang, D.; Paldi, R. L.; He, Z. H.; Lu, P.; Deitz, J.; Ahmad, A.; Dou, H. Y.; Wang, X. J.; Liu, J. C. et al. Abnormal in-plane epitaxy and formation mechanism of vertically aligned Au nanopillars in self-assembled CeO$_2$-Au metamaterial systems. *Mater. Horiz.* **2023**, *10*, 3101–3113.

[53] Huang, J. J.; Phuah, X. L.; McClintock, L. M.; Padmanabhan, P.; Vikrant, K. S. N.; Wang, H. H.; Zhang, D.; Wang, H.; Lu, P.; Gao, X. Y. et al. Core−shell metallic alloy nanopillars-in-dielectric hybrid metamaterials with magneto-plasmonic coupling. *Mater. Today* **2021**, *51*, 39–47.

[54] Zhang, D.; Misra, S.; Li, L. G.; Wang, X. J.; Jian, J.; Lu, P.; Gao, X. Y.; Sun, X.; Qi, Z. M.; Kalaswad, M. et al. Tunable optical properties in self-assembled oxide-metal hybrid thin films via Au-phase geometry control: From nanopillars to nanodisks. *Adv. Opt. Mater.* **2020**, *8*, 1901359.

[55] Whitney, T. M.; Searson, P. C.; Jiang, J. S.; Chien, C. L. Fabrication and magnetic properties of arrays of metallic nanowires. *Science* **1993**, *261*, 1316–1319.